THE JOURNAL OF PHYSICAL CHEMISTRY C
A JOURNAL OF THE AMERICAN CHEMICAL SOCIETY

pubs.acs.org/JPCC

Article

Ionic Liquid–Graphene Interface: Effect of Anions on the Fermi Level

Gangamallaiah Velpula,* Jian Xiang Lian, David Cornil, David Beljonne,* Roberto Lazzaroni, Kunal S. Mali, and Steven De Feyter*

Cite This: J. Phys. Chem. C 2023, 127, 12717–12726

Read Online

ACCESS | Metrics & More | Article Recommendations | Supporting Information

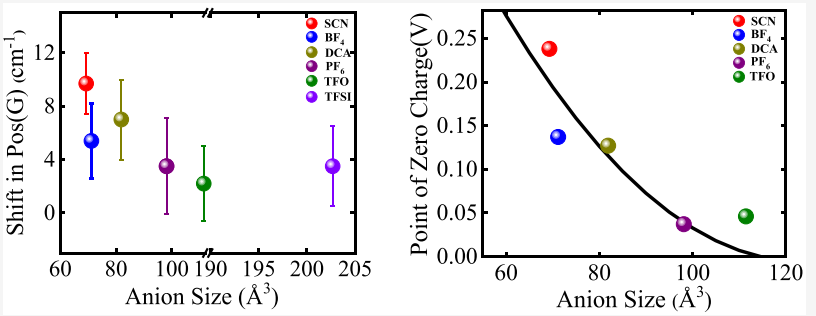

ABSTRACT: Since energy conversion and storage processes take place at the electrolyte–electrode interface, it is important to develop experimental and theoretical procedures to understand the interfacial nanostructure in graphene-based electrochemical storage devices where ionic liquids (ILs) are used as electrolytes. In this contribution, the impact of the anions of imidazolium-based ILs on the IL–graphene interface as well as on the electronic structure of graphene is investigated. Raman spectroscopy unveils that 1-butyl-3-methylimidazolium ILs having smaller anions induce n-type doping, while ILs with larger anions have a negligible effect on the doping. Molecular modeling simulations reveal that changes in the electrostatic potential at the IL–graphene interface are responsible for the n-type doping.

1. INTRODUCTION

Electrochemical energy storage devices have emerged as sustainable and reliable energy storage devices. Among all, rechargeable Li-ion batteries dominate the market due to their high energy density. However, the energy density of Li-ion batteries is size-dependent and decreases with the size of the battery. They also have other major disadvantages, including low power density, slower recharging rate, and limited battery life cycle. Therefore, researchers have been trying, on the one hand, to minimize the disadvantages of rechargeable batteries and, on the other hand, to develop alternative energy storage devices with high power and energy densities.[1−6]

Electrical double-layer (EDL) capacitors, also known as supercapacitors, have emerged as an alternative to rechargeable batteries due to their high power density, meaning they can deliver high amounts of energy in a short period of time. Supercapacitors can undergo more charge and discharge cycles than batteries, and as a consequence, have longer life cycles.[3,4] In addition, a supercapacitor stores and releases energy by the reversible desorption and adsorption of ions at the electrolyte–electrode interface. Thus, these devices are much safer than batteries. Furthermore, supercapacitors have a wide operating temperature range; therefore, they are not affected by thermal runaway and fire risk. However, the energy density of the supercapacitors is lower than the current rechargeable batteries. Therefore, the current research particularly aims at improving the energy density of supercapacitors. The energy density (E_D) of EDL capacitors is a function of the operating voltage (V_0) and the specific capacitance C of the electrode–electrolyte system and is given by $E_D = \xi \cdot C \cdot V_0^2$, where ξ is a constant. The specific capacitance mainly depends on the specific surface area (SSA) of an electrode. The operating voltage of the supercapacitor is controlled by the electrochemical window of an electrolyte. Furthermore, the energy conversion and storage processes take place at the electrode–electrolyte interface. Therefore, it is imperative to explore the interfacial structure of electrodes with a high SSA and electrolytes with a large electrochemical window.[5]

Graphene is a two-dimensional material with exceptional physicochemical and optoelectronic properties. Graphene electrodes have been widely used in various energy devices

Received: March 8, 2023
Revised: May 7, 2023
Published: June 22, 2023

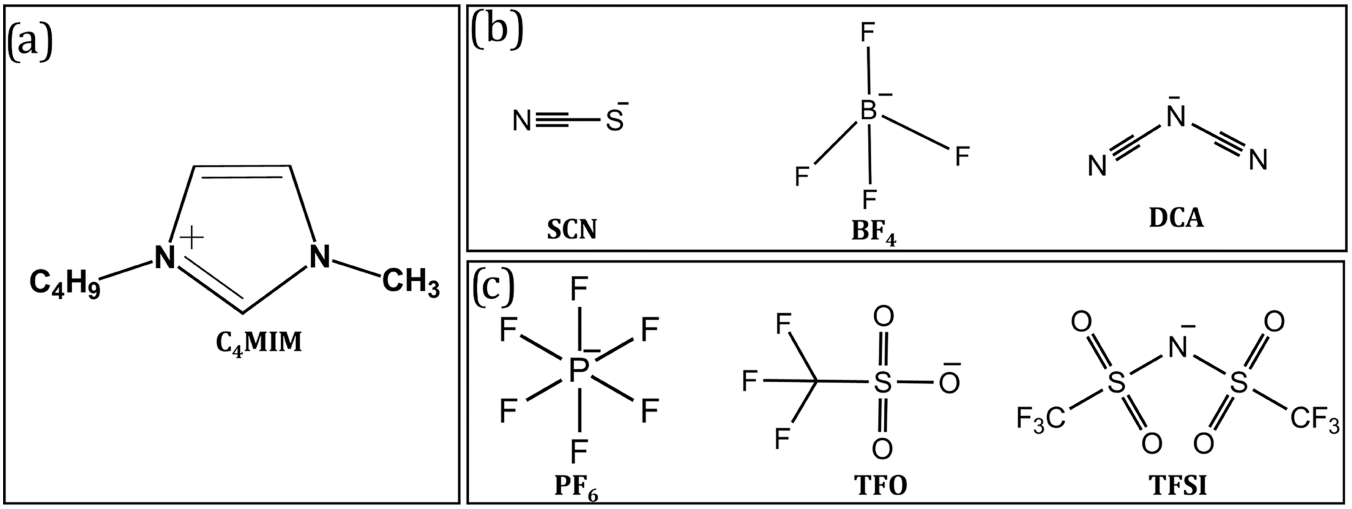

Figure 1. Chemical structure of the investigated ILs consisting of (a) an imidazolium cation with (b) small anions, including SCN, BF_4, and DCA, and (c) large anions, including PF_6, TFO, and TFSI.

due to their high specific surface area (2360 m^{-2} g).[7,8] Ionic liquids (ILs), on the other hand, possess wide electrochemical windows ranging between 4.5 and 5.0 V; in some cases, windows up to 6.0 V have been reported.[9,10] Besides the electrochemical windows, ILs also exhibit exceptional physicochemical properties, such as high thermal stability and low or negligible vapor pressure. In addition, their properties can be tuned for a desired application by varying the constituent ions (anions and cations) of the ILs.[11] Although the properties of graphene and ILs have been well-studied, the interfacial structure and its impact on graphene electronic structure are not completely understood yet.

Experimental probing of this interface is complicated by the complex interfacial structure of the IL−graphene, which is sustained by the coexistence of a multitude of interactions such as electrostatic, van der Waals, and hydrogen-bonding interactions. Therefore, it is important to use surface-sensitive techniques to characterize the interfacial nanostructure of ILs. Such techniques include sum-frequency generation (SFG),[12,13] X-ray reflectivity,[14] X-ray photoelectron spectroscopy (XPS),[15] reflection high-energy electron diffraction (RHEED),[16] atomic force microscopy (AFM),[17−19] and scanning tunneling microscopy (STM).[20] Recently, Welton and co-workers have summarized the typical length scale ordering in ILs proposed by various experimental methods.[21] The structure of ILs in contact with the electrode consists of three regimes: the electrical double layer, intermediate layer, and bulk IL. Surface-induced ordering of C_2MIM TFSI ILs has been studied by He et al. using RHEED.[16] They proposed that the cations and anions can only be influenced within 2 nm from the highly oriented pyrolytic graphite (HOPG) surface and form an ordered crystalline structure due to the lattice-matching effect. Therefore, not only interactions between ions of ILs are important but interactions between ions of ILs and the electrode surface are also important for the formation of extended ordered IL nanostructures. Although the nanostructure of ILs has been studied to some extent, the impact of the interfacial nanostructure on the electronic properties of the electrode (graphene) has not been explored. Dunsch and co-workers have studied the electrochemical doping of 1-butyl-3-methylimidazolium tetrafluoroborate on single-walled carbon nanotubes and fullerene peapods using Vis/NIR and Raman spectroelectrochemistry. The electrochemistry of both the nanotubes and peapods is dominated by their capacitive double-layer charging.[22] Therefore, comprehending the effect of ions of ILs on the electronic structure of graphene is particularly interesting in the context of further advancement of graphene as an electrode material.[22,23]

Recently, we have successfully employed Raman spectroscopy and theoretical calculations to understand the nanostructure of 1-alkyl-3-methylimidazolium tetrafluoroborate ILs (C_nMIM-BF_4, n = 2, 4, 6, 8, and 10) and its impact on graphene electronic structure.[24] It has been found that the length of the alkyl chain has a profound influence on the nanostructure of C_nMIM-BF_4 ILs and on graphene electronic structure. Adsorption of C_nMIM-BF_4 ILs leads to n-doping of graphene, and its magnitude increases with the length of the alkyl chain attached to the imidazolium cation. These previous results established that, although the negative charge is present on the anion of the IL, the cation can indeed change the interfacial nanostructure of ILs and, thus, influence the electronic structure of the graphene.

In this work, we report on the influence of various anions of ILs on the interfacial nanostructure and its impact on graphene electronic structure. The anions are known to play a significant role in intermolecular interactions, electrochemical properties, as well as physicochemical properties, such as conductivity, viscosity, and thermal stability.[25] Furthermore, a small variation in the IL composition has a dramatic effect on the interfacial nanostructure.[26−29] To correlate the impact of the anion on the interfacial nanostructure and the electronic structure of graphene, we have investigated the most commonly used cation, i.e., 1-butyl-3-methylimidazolium (C_4MIM), in combination with different anions, including thiocyanate (SCN), tetrafluoroborate (BF_4), dicyanamide (DCA), hexafluorophosphate (PF_6), triflate (TFO), and bis(trifluoromethanesulfonyl)imide (TFSI) (Figure 1). We provide a detailed account of the influence of IL adsorption on graphene using Raman spectroscopy and molecular dynamics (MD) simulations. Single-layer graphene (SLG) on SiO_2 was used as a substrate. Raman spectroscopy reveals that adsorption of ILs with small anions, i.e., C_4MIM-SCN, C_4MIM-BF_4, and C_4MIM-DCA, on graphene induces n-type doping of graphene and leads to lowering of the work function.

https://doi.org/10.1021/acs.jpcc.3c01602
J. Phys. Chem. C 2023, 127, 12717−12726

On the contrary, Raman spectra obtained after the deposition of ILs with larger anions (PF_6, TFO, and TFSI) indicate a negligible or limited alteration of the graphene electronic structure. A detailed discussion is provided for understanding the contrasting influence of small and large anions on the electronic structure of graphene.

2. METHODOLOGY

2.1. Experimental Details. *2.1.1. Raman Spectroscopy.* All of the ILs used in this study were purchased from IoLiTec-Ionic Liquids Technologies GmbH, and the stated purity of the ILs is >99.5%. Water content of the ionic liquids was estimated by Karl Fischer titration with the aid of Metrohm 831 KF Coulometer (Table S1 and Figure S1, Supporting Information). All of the ILs were used as received. CVD-grown graphene samples (1×1 cm^2) transferred to Si^{2+}/SiO_2 (300 nm) were obtained from Graphenea and were used as received. Raman experiments were performed at room temperature (21−23 °C) using an OmegaScopeTM 1000 (AIST-NT). Laser light from a He−Ne laser (632.8 nm) was reflected by using a dichroic mirror (Chroma, Z633RDC) and then focused onto the sample surface by using an objective (Mitutoyo, BD Plan Apo 100×, N.A. 0.7). The optical density at the sample surface was about 800 kW cm^{-2}. Raman scattering was collected with the same objective and directed to a Raman spectrograph (Horiba JY, iHR-320) equipped with a cooled charge-coupled device (CCD) camera operating at −100 °C (Andor, DU920P) through the dichroic mirror, a pinhole, and a long pass filter (Chroma, HQ645LP). Accumulation time for all spectra was 6 s. For each experiment, Raman maps were obtained for pristine as well as IL-functionalized graphene samples. A 10 μL drop of IL was placed onto a pristine graphene sample. The experiments were repeated in two or three sessions using different graphene samples for reproducibility and to avoid experimental artifacts, if any. Raman data were analyzed using MATLAB software.

2.2. Theoretical Methods. *2.2.1. Molecular Dynamics Approach.* Similar to the previous work,[24] the following models were built. We used a $29.925 \times 29.616 \times 40.000$ Å^3 simulation box containing C_4MIM-X pairs, where X is one of the different anions investigated in this work, sandwiched between two graphene sheets. In this model, the graphene layers were frozen during the molecular dynamics runs and simulated within periodic boundary conditions (PBC).

To describe the imidazolium-based cation and the anions at the classical level, we adopted the nonpolarizable force field proposed by Doherty, Acevedo, et al.[30] These force fields have been demonstrated to accurately reproduce several key thermodynamic properties, including experimental density, vaporization heat, ILs diffusion, and viscosity. The graphite layers were modeled as uncharged particles interacting with Lennard-Jones potential, corresponding to the sp^2 carbon atoms in the AMBER force field.[31] We used the Lorentz−Berthelot combination rule to handle the van der Waals (vdW) interactions between ILs and the graphite layers. The nonbonded interactions were treated using the cutoff method with a cutoff distance of 12 Å, and the long-range electrostatic interactions were handled in the reciprocal space using the particle mesh Ewald approach,[32] as implemented in the version 5.1.4 of the GROMACS software package.[33] We used an integration time step of 2 fs and applied C−H bond constraints with the LINCS algorithm.[34] Regarding the molecular dynamics (MD) simulations, we performed thermal annealing for 20 ns (NVT equilibration with the Berendsen thermostat and time constant of 0.5 ps), while decreasing the temperature from 1000 to 298 K. Subsequently, the systems were equilibrated with NPT ensemble, using both Berendsen and Parrinello−Rahman barostats (time constant of 5 ps) for 2 ns each. Then, the analyses were performed on a production MD trajectory of 20 ns at 450 K, using the Berendsen thermostat in the NVT ensemble.

The charge density distribution was calculated from the charge of the atoms and their average position (through the MD trajectory). The simulation box was divided along the z-direction into thin slices with $dz = 0.1$ Å, and the charge density was computed for each slice. The charge density distribution was then obtained as a function of z by using the gmx_density program implemented in GROMACS.

Assuming a planar capacitor, the electrostatic potential of the system can be calculated from the charge density distribution. The partial derivative of the potential with respect to the z-axis is the electric field intensity along the z-direction. According to Gauss's law, the electric field intensity of a charged plate is equal to the surface charge density divided by the vacuum permittivity. Therefore, the surface charge density of each small box can be obtained from the previously calculated charge density of each box multiplied by dz and assuming a uniform charge distribution. In this way, the profile of the electric field intensity can be calculated as a function of z. Eventually, the distribution of the electrostatic potential can be obtained by integrating the electric field intensity in the z-direction. This can be done using the gmx_potential command in GROMACS.

3. RESULTS AND DISCUSSION

Figure 1 shows the molecular structure of the ILs made of the 1-butyl-3-methylimidazolium cation (C_4MIM) and different anions (X = SCN, BF_4, DCA, PF_6, TFO, and TFSI) used in this study. These ILs are among the most commonly used ILs. Six different anions having different sizes were used. Such dissimilarities in size have a significant influence, in particular, on the electrostatic interactions between the ions of the ILs. These interactions define most of their physicochemical properties such as the conductivity and the viscosity to name a few.

3.1. Raman Characterization of the IL−Graphene Interface. The effect of anions of ILs on graphene has been investigated by observing the changes in the Raman spectrum of graphene before and after drop-casting neat ILs onto the surface. Raman spectroscopy is a nondestructive tool for the characterization of graphene. It has been used intensively to monitor the electronic structure of graphene and other properties such as the density of defects, electron density, number of layers, stress, and strain.[35] The primary Raman spectrum of graphene consists of three main bands: the G band (~1580 cm^{-1}), the D band (~1350 cm^{-1}), and the 2D band (~2650 cm^{-1}) found at the positions indicated by the excitation source used in this study. The relative shifts in the positions G [Pos(G)] and 2D [Pos(2D)] as well as their intensities can be used to understand the properties of graphene. The D band, which is the signature of defects in the lattice, helps as an indicator of crystallographic quality.[36] Definite evidence for changes in charge carrier concentration originates from the G and 2D bands. Under increasing n- or p-type doping, the G band upshifts, mainly due to the removal of a Kohn anomaly with which it is generally associated.[37] A

https://doi.org/10.1021/acs.jpcc.3c01602
J. Phys. Chem. C 2023, 127, 12717−12726

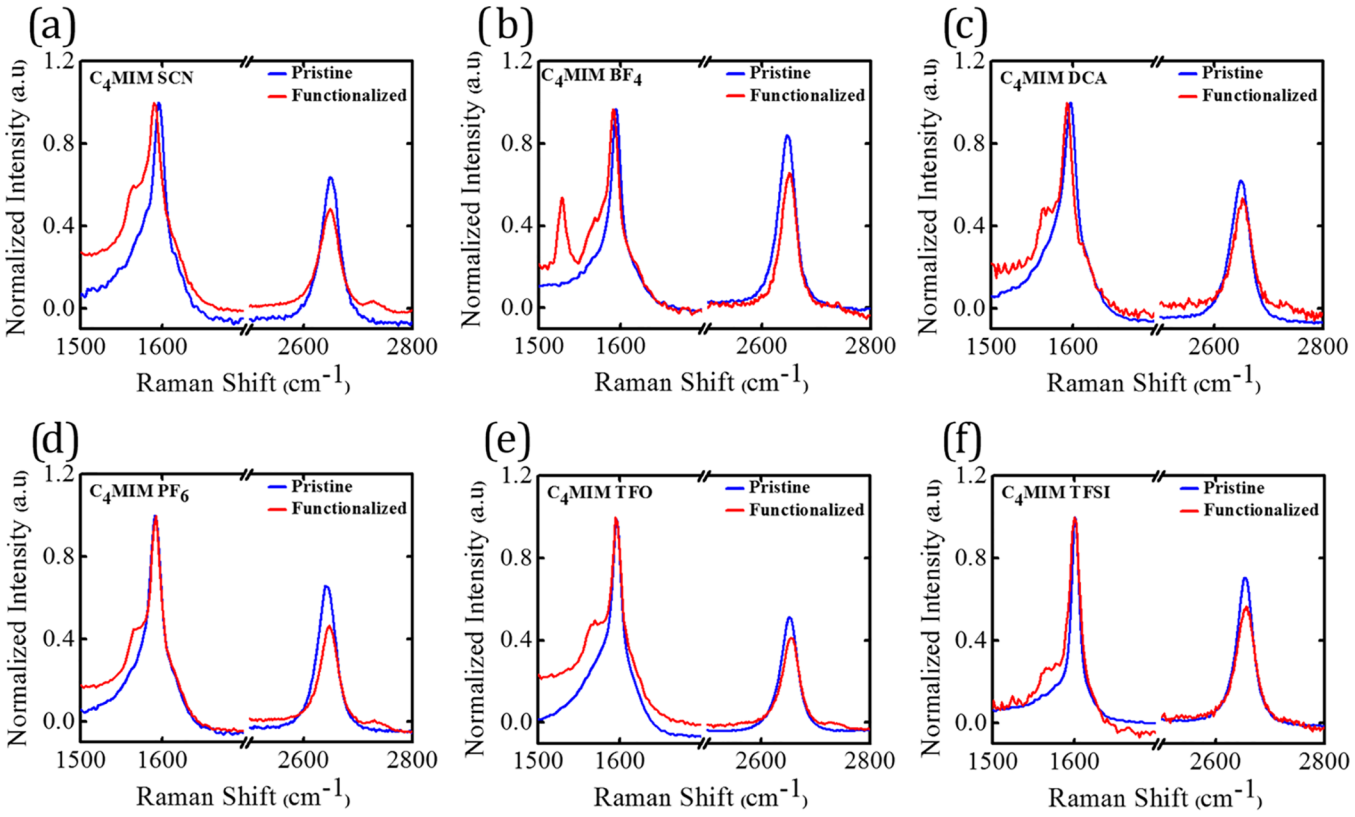

Figure 2. Normalized Raman spectra of graphene before and after functionalization with C_4MIM-X ILs. (Top) Typical Raman spectra before and after functionalization with smaller anions (a) C_4MIM-SCN, (b) C_4MIM-BF_4, and (c) C_4MIM-DCA. (Bottom) Typical Raman spectra before and after functionalization with larger anions (d) C_4MIM-PF_6, (e) C_4MIM-TFO, and (f) C_4MIM-TFSI. For the un-normalized Raman spectra, see Figure S2 in the Supporting Information.

Kohn anomaly occurs due to strong electron−phonon coupling and means that electrons can no longer fully relax during lattice vibrations, a phenomenon usually found in metals. Therefore, the expected position of the G band, Pos(G) for undoped graphene, is shifted to lower wavenumbers than expected in the absence of Kohn anomaly. However, the electron−phonon coupling becomes weaker upon doping and suppresses the Kohn anomaly leading to an upshift in the G band with increasing charge carrier concentration. For most levels of doping, this dominates any shift in Pos(G) that results from changes to the lattice constant. The 2D band, on the other hand, both decreases in intensity and shifts in position upon doping, effects that stem from Pauli blocking of the absorbed and/or emitted photons and changes in the lattice constant, respectively.[38] Electron doping serves to increase the lattice constant, and therefore leads to a downward shift of [Pos(2D)], while the opposite is true for hole doping. This indicates that the shift of the 2D band can in principle be used to distinguish between doping by different charge carriers.

3.2. Effect of Anions of ILs: Smaller vs Larger Anions.

Figure 2 displays Raman point spectra before and after the deposition of neat ILs having smaller anions (C_4MIM-SCN, C_4MIM-BF_4, and C_4MIM-DCA) and larger anions (C_4MIM-PF_6, C_4MIM-TFO, and C_4MIM-TFSI) on the surface of CVD-grown graphene transferred to SiO_2. For the six samples, Pos(G) is located around 1600 cm^{-1} before functionalization. In general, for charge-neutral graphene, Pos(G) is located around 1581 cm^{-1}. This indicates that the graphene samples used in this study are p-doped. This is due to the adsorption of water and oxygen mediated by a strong interaction with the SiO_2 substrate.[39] On the one hand, adsorption of water between the substrate and graphene has a significant effect on the electrical properties of graphene. However, understanding this effect is rather complex.[40] On the other hand, dry oxygen dopes reversibly, however, in the presence of water, and over long periods of time, the doping becomes stronger and irreversible. This is due to the stabilization of molecular oxygen anions via solvation by water and the resultant electrostatic binding to the SiO_2.[39] The intensity peak ratio of the D and G bands (I_D/I_G) indicates that the pristine graphene samples are of good quality; that is, the defect density is low. Upon deposition of neat ILs, additional peaks located between 1300 and 1575 cm^{-1} appear in the Raman spectrum (Figure S3, Supporting Information). These additional peaks are associated with the imidazolium ring and aliphatic chain vibrations of the C_nMIM cation.[23] These assignments were validated by performing Raman measurements on the bulk IL sample (C_4MIM-BF_4) (Figure S4, Supporting Information) and indicate that there is no/limited convolution with the native bands of graphene.

Interestingly, the Raman spectra obtained after functionalization of ILs having smaller anions (C_4MIM-SCN, C_4MIM-BF_4, and C_4MIM-DCA) show a shift of Pos(G) to lower wavenumbers relative to the pristine (unfunctionalized) graphene. The shifts observed for smaller anions (C_4MIM-SCN, C_4MIM-BF_4, and C_4MIM-DCA) are higher than those for larger anions (C_4MIM-PF_6, C_4MIM-TFO, and C_4MIM-TFSI). Furthermore, the intensity ratio of the G and 2D band (I_{2D}/I_G) of smaller anions (SCN, BF_4, and DCA) is slightly

https://doi.org/10.1021/acs.jpcc.3c01602
J. Phys. Chem. C 2023, 127, 12717−12726

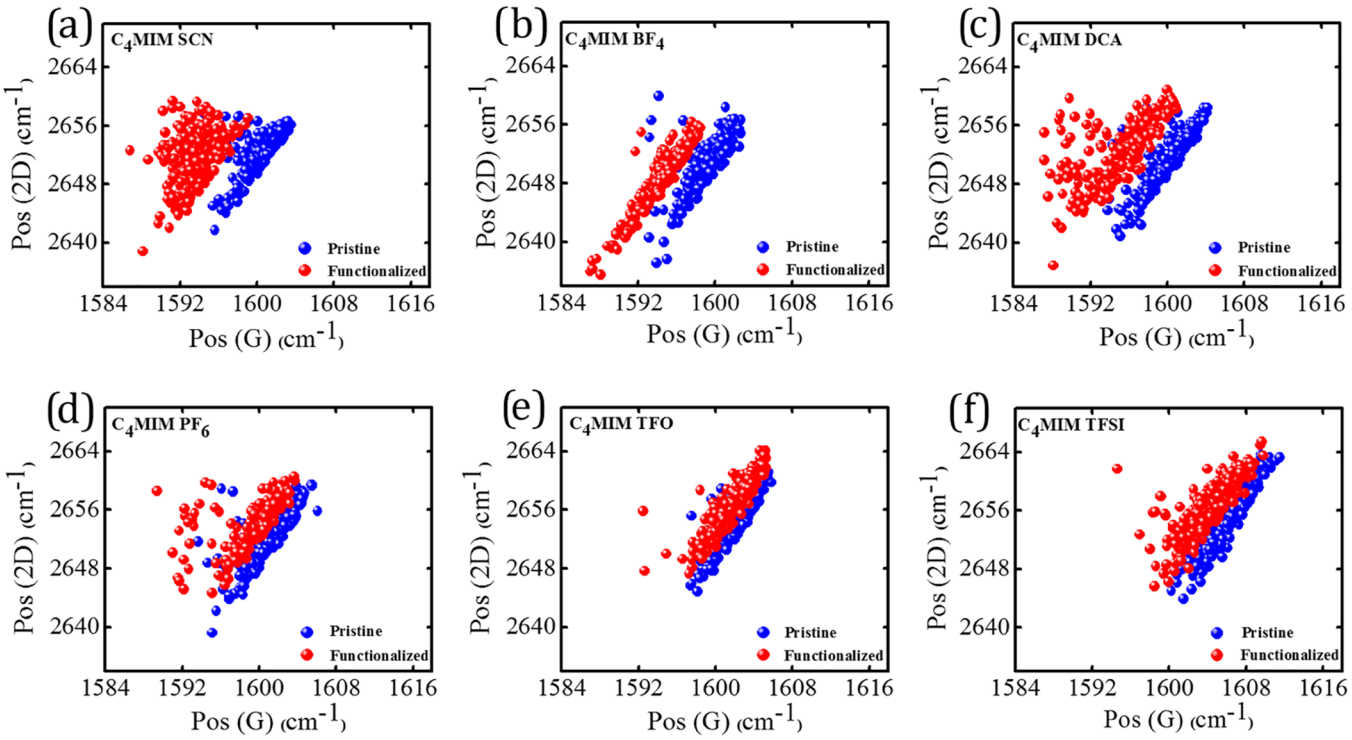

Figure 3. Plots of Pos(2D) versus Pos(G) for pristine and IL-functionalized graphene. (Top) Smaller anions: (a) C_4MIM-SCN, (b) C_4MIM-BF_4, and (c) C_4MIM-DCA. (Bottom) Larger anions: (d) C_4MIM-PF_6, (e) C_4MIM-TFO, and (f) C_4MIM-TFSI.

higher than the one of the larger anions (PF_6, TFO, and TFSI). These spectral changes clearly indicate a reduction in p-type doping, and therefore, it can be concluded that the ILs with the smaller anions, namely, C_4MIM-SCN, C_4MIM-BF_4, and C_4MIM-DCA, induce n-type doping of graphene. In the case of large-size anions (C_4MIM-PF_6, C_4MIM-TFO, and C_4MIM-TFSI), no significant shift of Pos(G) to lower wavenumbers relative to the pristine graphene was observed. This indicates that the larger anions cause negligible doping of graphene.

To quantify the extent of doping, Raman maps were recorded (10×10 μm^2 in size containing 10×10 pts^2) at three different positions, separated at least by several hundreds of micrometers, for each sample before and after functionalization. As stated above, the parameters in the Raman spectrum of graphene that depend on the charge carrier concentration are the positions of the G and 2D bands, their relative intensities, and the full width at half-maximum of the G band [FWHM(G)]. Observing these changes is normally complicated by other interfering factors such as the presence of defects, bilayers, substrate-induced mechanical strain, etc. Therefore, to separate the influence of these factors, the Raman data were analyzed in line with established protocols and details reported elsewhere.[24,41,42]

Figure 3a–c displays plots of Pos(2D) versus Pos(G) before and after deposition of C_4MIM-SCN, C_4MIM-BF_4, and C_4MIM-DCA ILs. Before IL deposition, Pos(G) is located around 1600 cm^{-1}. These results indicate a uniform amount of p-type doping and large variations in strain along the surface. After deposition of C_4MIM-SCN, C_4MIM-BF_4, and C_4MIM-DCA ILs, the data points shift to lower values of Pos(G) for all IL derivatives, while maintaining a similar variation in the strain. This downshift of Pos(G) indicates a reduction in p-type doping and again confirms that C_4MIM-SCN, C_4MIM-BF_4, and C_4MIM-DCA ILs cause n-type doping of graphene. Comparison of the shifts of Pos(G) for the different ILs clearly indicates that the n-type doping is higher for the ILs having small anions (C_4MIM-SCN, C_4MIM-BF_4, and C_4MIM-DCA) compared to the ILs with the larger anions (C_4MIM-PF_6, C_4MIM-TFO, and C_4MIM-TFSI (see Figure 3d–f)). The data are summarized in Table S2 in the Supporting Information.

Recently, we demonstrated that the n-type doping of graphene caused by C_nMIM BF_4 (n = 2, 4, 6, 8, and 10) ILs increases with an increase in the alkyl chain length (cation size).[24] These results are in contrast to those where the n-type doping of graphene caused by aliphatic primary amines was found to decrease with an increasing chain length of the aliphatic amines.[41] The contrasting results appear to originate from the different doping mechanisms. The density of alkyl amines adsorbed per unit area is reduced as a function of increase in the chain length, since for such systems, alkyl chains are known to adsorb parallel to the graphene surface.[43] As a consequence, the amount of doping is reduced with increasing chain length. However, in the case of imidazolium-based ILs, n-type doping increases with increasing chain length. To explain these results, we used molecular dynamic (MD) simulations, which revealed that the doping originates from the changes in the electrostatic potential at the IL–graphene interface. The alkyl chains introduce a charge screening effect on the graphene surface, which repels the anions from the surface to the bulk. This results in a net drop of the electrostatic potential near the interface, with a magnitude that scales with the length of the alkyl side chains.[24]

Figure 4 shows the shift in Pos(G) versus the anion size of the six anions used in this study.

The size of the six anions used in this study is taken from a previous literature report.[44] The amount of doping increases with decreasing size of anions. Note that the TFSI anion deviates from this trend. A detailed discussion is provided in

https://doi.org/10.1021/acs.jpcc.3c01602
J. Phys. Chem. C 2023, 127, 12717–12726

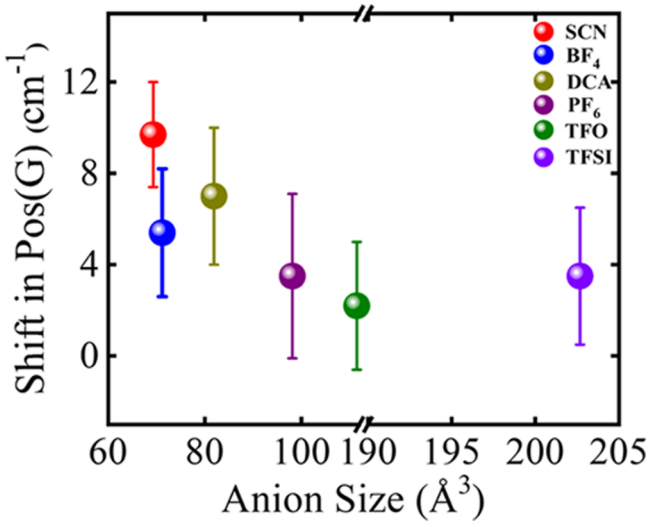

Figure 4. Shift in Pos(G) versus anion size. The data points reveal that the shift in Pos(G), which is indicative of the extent of doping, decreases with increasing size of anions except for the TFSI anion.

Section 3.3. To further comprehend the exact amount of doping, the number of injected electrons and Fermi level shifts have been estimated for all of the anions (Table S3 in the Supporting Information). Strain-corrected values of Pos(G) (Table S4) and the method reported by Ryu et al.[42] were used to estimate the number of injected electrons. Furthermore, the shift in Fermi level is calculated using the relation $E_f = \hbar\nu_f\sqrt{n\pi}$, where ν_f is the Fermi velocity (10^{-6} ms^{-1}) and n is the charge carrier concentration. Figure 5 displays the charge carrier concentration, i.e., the number of injected electrons per squared cm, and the Fermi level shift versus anion size.

The shift in the Fermi level decreases as the size of the anion increases except for TFSI. These results indicate that the n-doping effect becomes stronger as the size of the anion decreases. The size of the anion has a significant influence on the ILs conductivity and thus on the electrochemical behavior of graphene sheets. Recently, the electrochemical capacitive properties of graphene sheets in 1-ethyl-3-methylimidazolium cation (C_2MIM) having different anions (DCA, BF_4, and TFSI) have been investigated.[25] Graphene sheets in DCA show high specific capacitance because of the lowest viscosity, ion size, and molecular weight of C_2MIM DCA IL.

From the above discussion, it is clear that the size of the cations and anions has a profound influence on the graphene electronic structure. Previously, we have shown that increasing the length of alkyl side chain attached to the imidazolium cation alters the electrostatic potential at the interface. As a result, the magnitude of the doping linearly scales with the length of the alkyl chain. By contrast, the doping level increases when the size of the anion decreases. We have used MD simulations to understand these results.

3.3. Molecular Modeling of the Graphene/IL Interface. The organization of the ions on graphene was investigated using MD simulations considering a model that implements periodic boundary conditions, i.e., 30 × 30 × 40 Å^3 IL-filled box sandwiched between two graphene flakes. Although this model is not directly representative of the actual experiments, it has been demonstrated that it allows for a validation of the classical electrostatic calculations against more reliable quantum-chemical results.

The calculated number density profiles of the cations and the anions of all of the investigated ILs are shown in Figure 6a. In line with our previous work[24] and other reports,[43,45] oscillations of the number density profiles are observed, which extend up to ∼15 Å from the graphene surface to the bulk, which indicates that ILs form a layered structure. This organization is clearly noticeable as the first number density peak is relatively well pronounced. The number density profile corresponding to the PF_6 anion reveals a sharp peak of the anion density close to the graphene surface. Additionally, because of the bulky size of the anion, the peak corresponding to PF_6 anion is slightly upshifted (by ∼0.5 Å) with respect to the density peak corresponding to the C_4MIM cation. This indicates that the PF_6 anions are not co-adsorbed with the

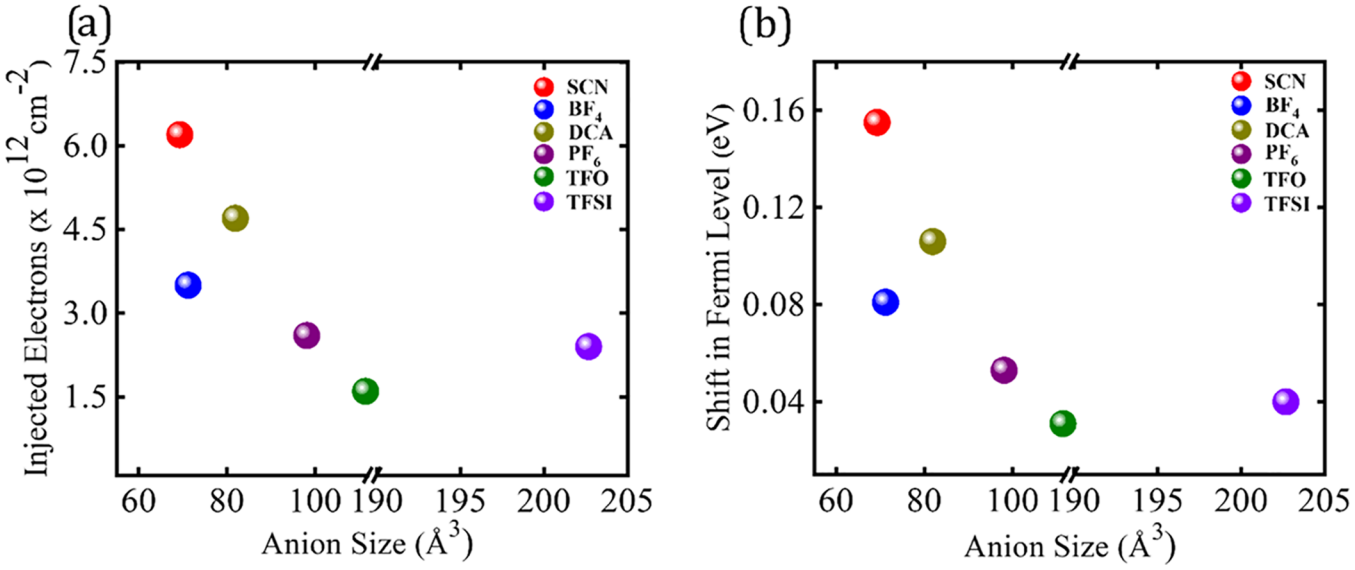

Figure 5. (a) Injected electrons versus anion size. (b) Fermi level shift versus anion size. The amount of doping and Fermi level shifts decrease with increasing anion size except for TFSI anion.

https://doi.org/10.1021/acs.jpcc.3c01602
J. Phys. Chem. C 2023, 127, 12717−12726

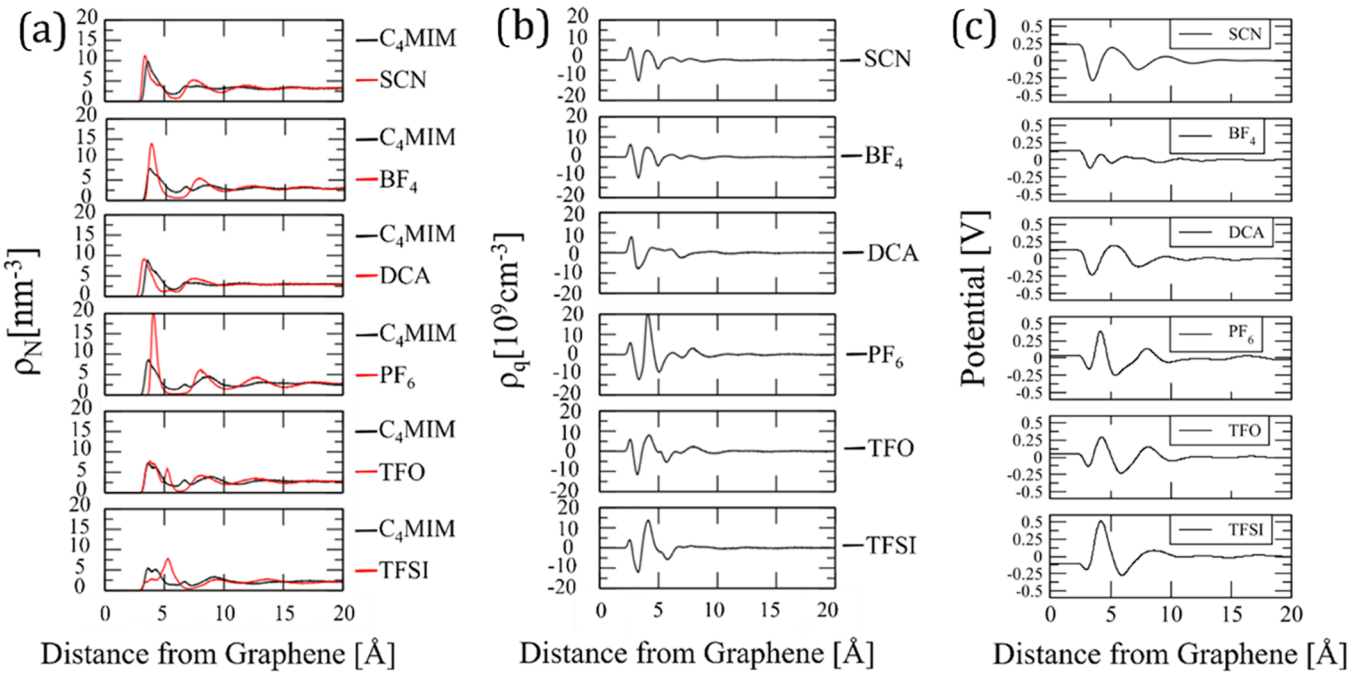

Figure 6. (a) Number density profile of C_4MIM-X ILs sandwiched between two graphene planes. The density profile of the cation (black lines) is calculated by the *z*-position of the nitrogen holding the alkyl chain, whereas the density profile of the anions (red lines) is given by the center of mass. (b) Charge density profiles along the *z*-axis of C_4MIM-X ILs at the graphene surface. (c) Surface electrostatic potential at the IL−graphene interface of the different C_4MIM-X ILs. The calculated potential profile is an average over both directions (upward and downward). The ZPC of each IL (average potential calculated in the region corresponding to the plateau in the middle of the box) is given in Table S5. For clarity, only the bottom half is shown.

cations. The latter are strongly adsorbed on the graphene surface, promoted by (i) the CH−π intermolecular interactions between the alkyl side chain and the graphite surface, leading to a favorable adsorption energy (while the unfavorable entropy loss at the interface is expected to have a minor effect in this case);[46] and (ii) the π-stacking interactions between the imidazolium ring of the cation and the graphene surface.[43] On the other hand, the number density profiles corresponding to the other anions reveal a superimposition of the first peaks corresponding to both the cation and the anion, indicating the co-adsorption of the cations and the anions (except C_4MIM-PF_6). The layering of the ILs at the graphene surface is still preserved in all cases.

Figure 6b shows the charge density profile of the ILs using a similar protocol as in ref 24 and detailed in Section 2. Since the bottom and top graphene layers are equivalent, the calculated profile reported in Figure 6b is an average of the surface charge density in both directions ("upward" and "downward"). As one moves away from the graphene surface, there is an accumulation of positive charge density associated with the cation, followed by a large peak at negative density due to the corresponding anions.

Because of the protective effect of the cation (see above), the anions are pulled away from the surface into the bulk. This results in a net drop of the electrostatic potential near the interface. More interestingly, the potential drop observed for all C_4MIM-X presents the following order with respect to the anion: SCN > DCA > BF_4 > PF_6 > TFO > TFSI (Figure 6c). We note that this hierarchy in the potential drop is in very good agreement with the experimental findings, which showed a Raman shift of the G peak in this respective order (Table S4 in the Supporting Information), the only exception being TFO and TFSI in reverse order. The deviation of TFSI is probably due to the reduced co-adsorption of TFSI and C_4MIM, compared to other anions. Figure 6a shows the density peak of C_4MIM at 0.3 nm above graphene, whereas the highest peak corresponding to TFSI is at >0.5 nm. Furthermore, the peak of C_4MIM is smaller in C_4MIM-TFSI, compared to other C_4MIM-X (X = SCN, DCA, BF_4, PF_6, and TFO) ILs.

We note that previous works reported on ILs made of C_4MIM-X, mainly for X = BF_4, PF_6, and TFSI. Namely, a supercapacitor consisting of a graphene electrode and C_4MIM-PF_6 IL was studied using DFT and a polarizable force field.[47] They reported that the IL−graphene interface exhibits an alternating cation/anion layering that extends to a few nanometers. Especially, the onset of the first number density peak (corresponding to F atoms of the PF_6 anion) is ∼0.5 Å closer to the surface, when compared to the position of the C_4MIM cation peak. On the other hand, in agreement with our MD simulations (Figure 6a), the peak intensity of the anion is almost double of that observed for the cation, which is due to the denser assembly of PF_6 anions at the graphene surface. Their reported electrostatic potential profile at zero applied voltage revealed the formation of a compact one-ion EDL, and the potential change is as low as 0.1 V, whereas our potential profiles extend over two ionic layers (1 nm above graphene), and the intensity of the variation can be as high as 0.35 V (Figure 6c). Nevertheless, the point of zero charge (PZC) is found to be almost 0 V, which agrees well with our data.

More recently, the interfacial structures of C_4MIM-BF_4 and C_4MIM-TFSI on graphene were investigated while changing the composition of the electrolyte and applying different potentials.[29] At zero voltage, the pure C_4MIM-BF_4 IL forms a concentrated inner layer (close to the graphene surface), consisting of the butyl functional group and the nonpolar trifluoromethyl group of the cation and anion, respectively.

https://doi.org/10.1021/acs.jpcc.3c01602
J. Phys. Chem. C 2023, 127, 12717−12726

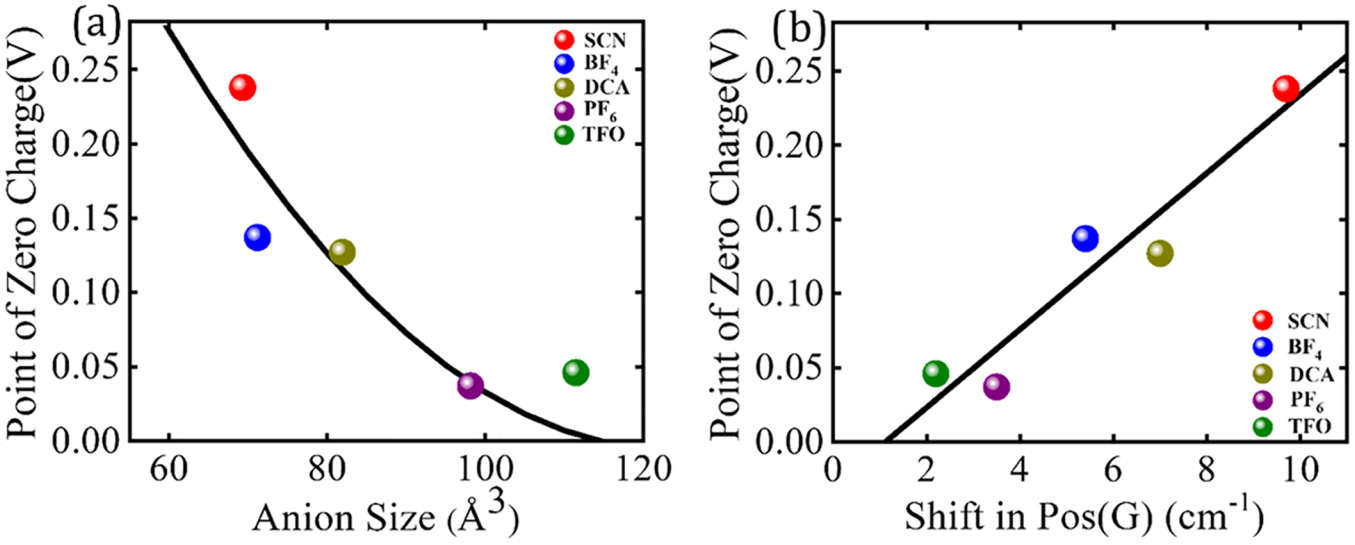

Figure 7. (a) Point of zero charge versus anion size of the different C_4MIM-X ILs. (b) Point of zero charge versus shift in Pos(G) of the different C_4MIM-X ILs. The lines passing through the data points represent a guide for the eye to follow the trends observed in this study.

Like PF_6 anions, the BF_4 anions form thin layered structures at the graphene surface. By contrast, the TFSI anions accumulate in thick ionic layers due to the more complex structure of TFSI, with CF_3 and SO_2 groups segregating into two distinct layers. Besides, Feng et al.[48] studied the effects of hydrophobicity/hydrophilicity of IL and applied voltage on the interfacial structure. Like previous work, they found a strong layered structure for C_4MIM-TFSI, with counterions accumulating at the surface, and the accumulations are greater at more positive voltage.

Overall, the abovementioned works reported the existence of a dense (or concentrated) layer of ions made of adsorbed cations and anions at ∼0.3 nm from the graphene surface. A second layer can also be formed, mostly by anions, and extend up to 1 nm from the graphene surface. Because of their steric differences, the anions can adsorb. The layering effect rules the charge density distribution at the electrode surface and capacitance, which can be tuned by properly selecting the counterions.

According to the experimental observations, the magnitude of doping increases with decreasing size of the anion. To further correlate the theoretical calculations with the experimental results, we have estimated the PZC, at which the electrostatic interactions between the graphene surface and the ILs are minimal (Table S5 in the Supporting Information). Figure 7 shows the variation of PZC as a function of anion size (Figure 7a) and shift in Pos(G) (Figure 7b). The PZC gradually increases with decreasing size of the anion. Furthermore, the PZC also varies proportionally to the experimentally observed shift in Pos(G) for all of the ILs used in the investigation. The PZC also follows the same hierarchy observed for the potential drop, the PZC being larger for the small anions than for the larger anions.

The results of the calculations are consistent with the observed experimental trend. This combined experimental and theoretical study gives a general understanding of how the anion affects the nanostructure in different IL systems and, on the other hand, how it impacts the electronic structure of graphene.

4. CONCLUSIONS

The graphene Fermi level was altered by the adsorption of ionic liquids based on the 1-butyl-3-methylimidazolium cation, and the impact of the nature and the size of six anions was compared. Raman spectroscopy and molecular dynamics simulations have been used to understand the impact of different anions on the electronic properties of graphene. The experimental results reveal that the charge carrier concentration increases with decreasing size of the anion. Classical MD simulations show that the n-type doping of graphene in contact with the ILs arises from the electrostatic layering effect.

These results highlight that a combined investigation of the electrolyte and electrode is necessary for developing safe and efficient graphene-based electrochemical energy storage devices such as supercapacitors. The results presented here are valuable for understanding the energy storage mechanism of IL−graphene-based electrochemical energy storage devices, in particular, supercapacitors. In addition, they also provide valuable information for selecting appropriate ILs and designing high-efficiency IL−graphene supercapacitors. However, apart from the fundamental aspects described above, various other factors need to be considered. For instance, the viscosity and the conductivity of ILs largely depend on the electrostatic interactions between anions and cations, and the length of the alkyl chain attached to either of the ions in the ILs. The size, shape, and molecular weight are also important factors in determining the electrical conductivity of ILs and other electrochemical parameters such as the electrochemical window of an electrolyte.

■ ASSOCIATED CONTENT

Supporting Information

The Supporting Information is available free of charge at https://pubs.acs.org/doi/10.1021/acs.jpcc.3c01602.

Additional Raman data and tables (number of injected electrons, Fermi level shifts, PZC values) (PDF)

https://doi.org/10.1021/acs.jpcc.3c01602
J. Phys. Chem. C 2023, 127, 12717−12726

AUTHOR INFORMATION

Corresponding Authors

Gangamallaiah Velpula − *Division of Molecular Imaging and Photonics, Department of Chemistry, KU Leuven, B-3001 Leuven, Belgium;* orcid.org/0000-0002-0642-6892; Email: gm.velpula@kuleuven.be

David Beljonne − *Laboratory for Chemistry of Novel Materials, Materials Research Institute, University of Mons, 7000 Mons, Belgium;* orcid.org/0000-0002-2989-3557; Email: david.beljonne@umons.ac.be

Steven De Feyter − *Division of Molecular Imaging and Photonics, Department of Chemistry, KU Leuven, B-3001 Leuven, Belgium;* orcid.org/0000-0002-0909-9292; Email: steven.defeyter@kuleuven.be

Authors

Jian Xiang Lian − *Computational Catalysis for Clean Energy, University of Calgary, Calgary T2N1N4 Alberta, Canada*

David Cornil − *Laboratory for Chemistry of Novel Materials, Materials Research Institute, University of Mons, 7000 Mons, Belgium;* orcid.org/0000-0002-9553-1626

Roberto Lazzaroni − *Laboratory for Chemistry of Novel Materials, Materials Research Institute, University of Mons, 7000 Mons, Belgium;* orcid.org/0000-0002-6334-4068

Kunal S. Mali − *Division of Molecular Imaging and Photonics, Department of Chemistry, KU Leuven, B-3001 Leuven, Belgium;* orcid.org/0000-0002-9938-6446

Complete contact information is available at: https://pubs.acs.org/10.1021/acs.jpcc.3c01602

Notes

The authors declare no competing financial interest.

ACKNOWLEDGMENTS

Financial support from the Research Foundation—Flanders (FWO G0A3220N) and KU Leuven—Internal Funds (C14/19/079) is acknowledged. This work was in part supported by FWO (G0H2122N, GF9118N) and F.R.S.-FNRS under the Excellence of Science EOS program (projects 30489208 and 40007495). The computational resources in Mons are supported by the FNRS "Consortium des Equipements de Calcul Intensif—CECI" program grant no. 2.5020.11 and by the Walloon Region (ZENOBE Tier-1 supercomputer, under grant 1117545). D.B. is a FNRS research director. G.V. acknowledges the FWO fellowship award (no. 1269221N). The authors also thank Roald Phillipson for insightful discussions.

REFERENCES

(1) Simon, P.; Gogotsi, Y. Materials for electrochemical capacitors. *Nat. Mater.* **2008**, *7*, 845.

(2) Tsai, W.-Y.; Lin, R.; Murali, S.; Li Zhang, L.; McDonough, J. K.; Ruoff, R. S.; Taberna, P.-L.; Gogotsi, Y.; Simon, P. Outstanding performance of activated graphene based supercapacitors in ionic liquid electrolyte from −50 to 80 °C. *Nano Energy* **2013**, *2*, 403−411.

(3) Simon, P.; Gogotsi, Y.; Dunn, B. Where Do Batteries End and Supercapacitors Begin? *Science* **2014**, *343*, 1210−1211.

(4) Lian, C.; Liu, K.; Van Aken, K. L.; Gogotsi, Y.; Wesolowski, D. J.; Liu, H. L.; Jiang, D. E.; Wu, J. Z. Enhancing the Capacitive Performance of Electric Double-Layer Capacitors with Ionic Liquid Mixtures. *ACS Energy Lett.* **2016**, *1*, 21−26.

(5) Wang, X.; Salari, M.; Jiang, D.-e.; Chapman Varela, J.; Anasori, B.; Wesolowski, D. J.; Dai, S.; Grinstaff, M. W.; Gogotsi, Y. Electrode material−ionic liquid coupling for electrochemical energy storage. *Nat. Rev. Mater.* **2020**, *5*, 787−808.

(6) McCloskey, B. D. Expanding the Ragone Plot: Pushing the Limits of Energy Storage. *J. Phys. Chem. Lett.* **2015**, *6*, 3592−3593.

(7) Raccichini, R.; Varzi, A.; Passerini, S.; Scrosati, B. The role of graphene for electrochemical energy storage. *Nat. Mater.* **2015**, *14*, 271.

(8) Bonaccorso, F.; Colombo, L.; Yu, G.; Stoller, M.; Tozzini, V.; Ferrari, A. C.; Ruoff, R. S.; Pellegrini, V. Graphene, related two-dimensional crystals, and hybrid systems for energy conversion and storage. *Science* **2015**, *347*, No. 1246501.

(9) Mousavi, M. P. S.; Wilson, B. E.; Kashefolgheta, S.; Anderson, E. L.; He, S.; Bühlmann, P.; Stein, A. Ionic Liquids as Electrolytes for Electrochemical Double-Layer Capacitors: Structures that Optimize Specific Energy. *ACS Appl. Mater. Interfaces* **2016**, *8*, 3396−3406.

(10) Hapiot, P.; Lagrost, C. Electrochemical Reactivity in Room-Temperature Ionic Liquids. *Chem. Rev.* **2008**, *108*, 2238−2264.

(11) Fedorov, M. V.; Kornyshev, A. A. Ionic Liquids at Electrified Interfaces. *Chem. Rev.* **2014**, *114*, 2978−3036.

(12) Xu, S.; Xing, S.; Pei, S.-S.; Ivaništšev, V.; Lynden-Bell, R.; Baldelli, S. Molecular Response of 1-Butyl-3-Methylimidazolium Dicyanamide Ionic Liquid at the Graphene Electrode Interface Investigated by Sum Frequency Generation Spectroscopy and Molecular Dynamics Simulations. *J. Phys. Chem. C* **2015**, *119*, 26009−26019.

(13) Xu, S.; Xing, S.; Pei, S.-S.; Baldelli, S. Sum Frequency Generation Spectroscopy Study of an Ionic Liquid at a Graphene-BaF2 (111) Interface. *J. Phys. Chem. B* **2014**, *118*, 5203−5210.

(14) Mezger, M.; Schröder, H.; Reichert, H.; Schramm, S.; Okasinski, J. S.; Schöder, S.; Honkimäki, V.; Deutsch, M.; Ocko, B. M.; Ralston, J.; Rohwerder, M.; Stratmann, M.; Dosch, H. Molecular Layering of Fluorinated Ionic Liquids at a Charged Sapphire (0001) Surface. *Science* **2008**, *322*, 424−428.

(15) Steinrück, H.-P. Recent developments in the study of ionic liquid interfaces using X-ray photoelectron spectroscopy and potential future directions. *Phys. Chem. Chem. Phys.* **2012**, *14*, 5010−5029.

(16) He, X.; Wu, C.; Rajagopal, K.; Punpongjareorn, N.; Yang, D.-S. Ordered ionic liquid structure observed at terraced graphite interfaces. *Phys. Chem. Chem. Phys.* **2016**, *18*, 3392−3396.

(17) Elbourne, A.; McDonald, S.; Voïchovsky, K.; Endres, F.; Warr, G. G.; Atkin, R. Nanostructure of the Ionic Liquid−Graphite Stern Layer. *ACS Nano* **2015**, *9*, 7608−7620.

(18) Hayes, R.; Warr, G. G.; Atkin, R. Structure and Nanostructure in Ionic Liquids. *Chem. Rev.* **2015**, *115*, 6357−6426.

(19) Black, J. M.; Zhu, M.; Zhang, P.; Unocic, R. R.; Guo, D.; Okatan, M. B.; Dai, S.; Cummings, P. T.; Kalinin, S. V.; Feng, G.; Balke, N. Fundamental aspects of electric double layer force-distance measurements at liquid-solid interfaces using atomic force microscopy. *Sci. Rep.* **2016**, *6*, No. 32389.

(20) Buchner, F.; Forster-Tonigold, K.; Bozorgchenani, M.; Gross, A.; Behm, R. J. Interaction of a Self-Assembled Ionic Liquid Layer with Graphite(0001): A Combined Experimental and Theoretical Study. *J. Phys. Chem. Lett.* **2016**, *7*, 226−233.

(21) Toda, S.; Clark, R.; Welton, T.; Shigeto, S. Observation of the Pockels Effect in Ionic Liquids and Insights into the Length Scale of Potential-Induced Ordering. *Langmuir* **2021**, *37*, 5193−5201.

(22) Kavan, L.; Dunsch, L. Ionic Liquid for in situ Vis/NIR and Raman Spectroelectrochemistry: Doping of Carbon Nanostructures. *ChemPhysChem* **2003**, *4*, 944−950.

(23) Mahurin, S. M.; Surwade, S. P.; Crespo, M.; Dai, S. Probing the interaction of ionic liquids with graphene using surface-enhanced Raman spectroscopy. *J. Raman Spectrosc.* **2016**, *47*, 585−590.

(24) Velpula, G.; Phillipson, R.; Lian, J. X.; Cornil, D.; Walke, P.; Verguts, K.; Brems, S.; Uji-i, H.; De Gendt, S.; Beljonne, D.; Lazzaroni, R.; Mali, K. S.; De Feyter, S. Graphene Meets Ionic Liquids: Fermi Level Engineering via Electrostatic Forces. *ACS Nano* **2019**, *13*, 3512−3521.

(25) Shi, M.; Kou, S.; Yan, X. Engineering the Electrochemical Capacitive Properties of Graphene Sheets in Ionic-Liquid Electrolytes by Correct Selection of Anions. *ChemSusChem* **2014**, *7*, 3053−3062.
(26) Gebbie, M. A.; Smith, A. M.; Dobbs, H. A.; Lee, A. A.; Warr, G. G.; Banquy, X.; Valtiner, M.; Rutland, M. W.; Israelachvili, J. N.; Perkin, S.; Atkin, R. Long range electrostatic forces in ionic liquids. *Chem. Commun.* **2017**, *53*, 1214−1224.
(27) Cook, A.; Ueno, K.; Watanabe, M.; Atkin, R.; Li, H. Effect of Variation in Anion Type and Glyme Length on the Nanostructure of the Solvate Ionic Liquid/Graphite Interface as a Function of Potential. *J. Phys. Chem. C* **2017**, *121*, 15728−15734.
(28) Liu, X.; Wang, Y.; Li, S.; Yan, T. Effects of anion on the electric double layer of imidazolium-based ionic liquids on graphite electrode by molecular dynamics simulation. *Electrochim. Acta* **2015**, *184*, 164−170.
(29) Tu, Y.-J.; McDaniel, J. G. Structure−Capacitance Relationships of Graphene/Ionic Liquid Electrolyte Double Layers. *J. Phys. Chem. C* **2021**, *125*, 20204−20218.
(30) Doherty, B.; Zhong, X.; Gathiaka, S.; Li, B.; Acevedo, O. Revisiting OPLS Force Field Parameters for Ionic Liquid Simulations. *J. Chem. Theory Comput.* **2017**, *13*, 6131−6145.
(31) Cornell, W. D.; Cieplak, P.; Bayly, C. I.; Gould, I. R.; Merz, K. M.; Ferguson, D. M.; Spellmeyer, D. C.; Fox, T.; Caldwell, J. W.; Kollman, P. A. A Second Generation Force Field for the Simulation of Proteins, Nucleic Acids, and Organic Molecules. *J. Am. Chem. Soc.* **1995**, *117*, 5179−5197.
(32) Essmann, U.; Perera, L.; Berkowitz, M. L.; Darden, T.; Lee, H.; Pedersen, L. G. A smooth particle mesh Ewald method. *J. Chem. Phys.* **1995**, *103*, 8577−8593.
(33) Van Der Spoel, D.; Lindahl, E.; Hess, B.; Groenhof, G.; Mark, A. E.; Berendsen, H. J. C. GROMACS: Fast, flexible, and free. *J. Comput. Chem.* **2005**, *26*, 1701−1718.
(34) Hess, B. P-LINCS: A Parallel Linear Constraint Solver for Molecular Simulation. *J. Chem. Theory Comput.* **2008**, *4*, 116−122.
(35) Ferrari, A. C.; Basko, D. M. Raman spectroscopy as a versatile tool for studying the properties of graphene. *Nat. Nanotechnol.* **2013**, *8*, 235−246.
(36) Niyogi, S.; Bekyarova, E.; Itkis, M. E.; Zhang, H.; Shepperd, K.; Hicks, J.; Sprinkle, M.; Berger, C.; Lau, C. N.; deHeer, W. A.; Conrad, E. H.; Haddon, R. C. Spectroscopy of Covalently Functionalized Graphene. *Nano Lett.* **2010**, *10*, 4061−4066.
(37) Pisana, S.; Lazzeri, M.; Casiraghi, C.; Novoselov, K. S.; Geim, A. K.; Ferrari, A. C.; Mauri, F. Breakdown of the adiabatic Born−Oppenheimer approximation in graphene. *Nat. Mater.* **2007**, *6*, 198.
(38) Das, A.; Pisana, S.; Chakraborty, B.; Piscanec, S.; Saha, S. K.; Waghmare, U. V.; Novoselov, K. S.; Krishnamurthy, H. R.; Geim, A. K.; Ferrari, A. C.; Sood, A. K. Monitoring dopants by Raman scattering in an electrochemically top-gated graphene transistor. *Nat. Nanotechnol.* **2008**, *3*, 210.
(39) Ryu, S.; Liu, L.; Berciaud, S.; Yu, Y.-J.; Liu, H.; Kim, P.; Flynn, G. W.; Brus, L. E. Atmospheric Oxygen Binding and Hole Doping in Deformed Graphene on a SiO2 Substrate. *Nano Lett.* **2010**, *10*, 4944−4951.
(40) Koyama, T.; Inaba, T.; Komatsu, K.; Moriyama, S.; Shimizu, M.; Homma, Y. Effect of interfacial water formed between graphene and SiO2/Si substrate. *Appl. Phys. Express* **2017**, *10*, No. 075102.
(41) Phillipson, R.; Lockhart de la Rosa, C. J.; Teyssandier, J.; Walke, P.; Waghray, D.; Fujita, Y.; Adisoejoso, J.; Mali, K. S.; Asselberghs, I.; Huyghebaert, C.; Uji-i, H.; De Gendt, S.; De Feyter, S. Tunable doping of graphene by using physisorbed self-assembled networks. *Nanoscale* **2016**, *8*, 20017−20026.
(42) Lee, J. E.; Ahn, G.; Shim, J.; Lee, Y. S.; Ryu, S. Optical separation of mechanical strain from charge doping in graphene. *Nat. Commun.* **2012**, *3*, No. 1024.
(43) Wang, S.; Li, S.; Cao, Z.; Yan, T. Molecular Dynamic Simulations of Ionic Liquids at Graphite Surface. *J. Phys. Chem. C* **2010**, *114*, 990−995.
(44) Zhu, P.; Kang, X.; Latif, U.; Gong, M.; Zhao, Y. A Reliable Database for Ionic Volume and Surface: Its Application To Predict Molar Volume and Density of Ionic Liquid. *Ind. Eng. Chem. Res.* **2019**, *58*, 10073−10083.
(45) Jo, S.; Park, S.-W.; Shim, Y.; Jung, Y. Effects of Alkyl Chain Length on Interfacial Structure and Differential Capacitance in Graphene Supercapacitors: A Molecular Dynamics Simulation Study. *Electrochim. Acta* **2017**, *247*, 634−645.
(46) Haar, S.; Bruna, M.; Lian, J. X.; Tomarchio, F.; Olivier, Y.; Mazzaro, R.; Morandi, V.; Moran, J.; Ferrari, A. C.; Beljonne, D.; Ciesielski, A.; Samorì, P. Liquid-Phase Exfoliation of Graphite into Single- and Few-Layer Graphene with α-Functionalized Alkanes. *J. Phys. Chem. Lett.* **2016**, *7*, 2714−2721.
(47) Paek, E.; Pak, A. J.; Hwang, G. S. A Computational Study of the Interfacial Structure and Capacitance of Graphene in [BMIM][PF6] Ionic Liquid. *J. Electrochem. Soc.* **2013**, *160*, A1.
(48) Bi, S.; Wang, R.; Liu, S.; Yan, J.; Mao, B.; Kornyshev, A. A.; Feng, G. Minimizing the electrosorption of water from humid ionic liquids on electrodes. *Nat. Commun.* **2018**, *9*, No. 5222.

https://doi.org/10.1021/acs.jpcc.3c01602
J. Phys. Chem. C 2023, 127, 12717−12726